Journal of Electronic Materials (2022) 51:769–777
https://doi.org/10.1007/s11664-021-09357-x

ORIGINAL RESEARCH ARTICLE

Synergistic Coupling of High Capacity $Li_{1.2}Mn_{0.54}Ni_{0.13}Co_{0.13}O_2$ and High Voltage $LiMn_{1.6}Ni_{0.4}O_4$ Lithium-Ion Battery Cathodes

Muharrem Kunduraci[1] · Rojbin Buluttekin[2] · Rasiha Nefise Mutlu[2] · Ahmet Murat Gizir[2]

Received: 18 August 2021 / Accepted: 16 November 2021 / Published online: 3 January 2022

Abstract

Manganese−based cathode materials are good alternatives to nickel-based layered cathodes in lithium-ion batteries due to the much cheaper cost of manganese ores. Coprecipitation is a popular method to produce precursor materials for lithium-ion batteries since its versatility enables the synthesis of a wide range of compositions with various architectures. In this study, spherical 2-µm to 4-µm-diameter binary $Mn_{0.8}Ni_{0.2}CO_3$ and ternary $Mn_{4/6}Ni_{1/6}Co_{1/6}CO_3$ precursor materials were synthesized by tuning synthesis conditions including temperature, feeding mode and reagent quantity. The binary and ternary precursor materials were mixed and reacted with Li_2CO_3 at 800°C to obtain $LiMn_{1.6}Ni_{0.4}O_4$ and $Li_{1.2}Mn_{0.54}Ni_{0.13}Co_{0.13}O_2$ cathode materials, respectively. $LiMn_{1.6}Ni_{0.4}O_4$ had a discharge capacity of 132 mAh g^{-1} and exhibited excellent cycle life and voltage retention. On the other hand, 221 mAh g^{-1} discharge capacity was achieved with $Li_{1.2}Mn_{0.54}Ni_{0.13}Co_{0.13}O_2$, but it showed a fast capacity and voltage decay. A hybrid electrode made of 50:50 wt% of both cathodes yielded 166 mAh g^{-1} capacity and 3.95 V average discharge voltage with much reduced voltage decay and capacity fading rate, thereby mitigating each other's weakness in the process.

Graphical Abstract

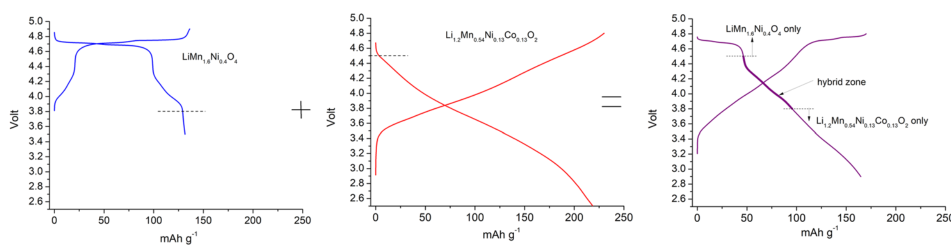

Keywords Coprecipitation · battery · cathode · spherical

Introductıon

Lithium-ion batteries are currently the leading electrochemical energy storage technology and are expected to continue their rein in the future thanks to their high energy density, cycle life and reliability[1–7] $LiNi_xMn_yCo_{1-x-y}O_2$ and $LiNi_{0.80}Co_{0.15}Al_{0.05}O_2$ are the state-of-the-art cathode materials currently used in electric vehicles and portable electronics. However, there have been significant efforts particularly in the last decade to replace them with cheaper and higher energy density alternatives. High lithium capacity layered–layered-type $(x)Li_2MnO_3$-$(1-x)LiMO_2$ (M=Mn, Co, Ni) composite cathodes and high-voltage spinel $LiMn_{1.5+x}Ni_{0.5-x}O_4$ cathodes stand out thanks to their low material cost and easy synthesis.[8–12]

While $(x)Li_2MnO_3$-$(1-x)LiMO_2$ cathodes offer discharge capacities in excess of 220 mAh g^{-1}, they are known to suffer from voltage decay with cycling as a result of surface degradation and atomic rearrangements.[13,14] Also, even though they are typically charged to 4.8 V, their discharge

✉ Muharrem Kunduraci
kunduraci.m@hotmail.com

1 Department of Aerospace Engineering, Tarsus University, Mersin, Turkey

2 Department of Chemistry, Mersin University, Mersin, Turkey

capacity within the 4.4–4.8 V range is only a fraction of their overall capacity due to as much as 0.4 V hysteresis in their voltage curves. This results in very poor energy efficiency for the layered–layered cathode. On the other hand, $LiMn_{1.6}Ni_{0.4}O_4$ operates within this mentioned potential range with good cyclability and voltage efficiency. Therefore, combining these two cathodes in a single electrode could create a high energy density cathode with good cycle life and energy efficiency. Given that these two cathode materials have similar chemical fingerprints, a single synthesis method could suit both of them.

In this study, we synthesized $Li_{1.2}Mn_{0.54}Ni_{0.13}Co_{0.13}O_2$ ($0.5Li_2MnO_3$-$0.5LiNi_{1/3}Mn_{1/3}Co_{1/3}O_2$) and $LiMn_{1.6}Ni_{0.4}O_4$ cathode materials using a coprecipitation method. Coprecipitation synthesis was chosen since it allows good chemistry and morphology control. The synthesis is based on the supersaturation of a solution with transition metal ions (e.g. Mn^{+2}, Ni^{+2} or Co^{+2}) and carbonate (CO_3^{-2}) ions and the emergence of insoluble metal carbonate nuclei. As these nuclei collide with each other in solution, some of these collisions result in the bonding of nuclei in a process called coalescence. If enough time is provided, these nuclei are chemically merged thanks to solid-state atomic diffusion, thereby resulting in larger particles. As the synthesis progresses, the collision-coalescence mechanism produces spherical particles several micrometers in diameter. Initially, we started with the synthesis of binary $Mn_{0.8}Ni_{0.2}CO_3$ precursor material and studied the impacts of temperature, feeding mode and reagent quantity on its final physical and chemical characteristics. Once the best conditions to produce spherical precursor materials without significant agglomeration were identified, they were applied to the synthesis of ternary ($Mn_{4/6}Ni_{1/6}Co_{1/6}$)CO_3 precursor material. $LiMn_{1.6}Ni_{0.4}O_4$ and $Li_{1.2}Mn_{0.54}Ni_{0.13}Co_{0.13}O_2$ cathode materials obtained from these precursors were later tested both individually and in a 50:50 wt% mixture for their lithium storage capacities and cyclability.

Experimental

Preparation of Metal Carbonate Precursors

In order to prepare the metal carbonate battery precursors, a total of 0.02 mole of metal sulfate salts ($MnSO_4 \cdot H_2O$, $NiSO_4 \cdot 6H_2O$, $CoSO_4 \cdot 7H_2O$) was dissolved in deionized (DI) water (solution A). The total volume of the solution was adjusted to 10 mL. In another solution, 2.72 g of $Na_2CO_3 \cdot H_2O$ (=0.022 mole) was dissolved in DI water with the total volume again adjusted to 10 mL (solution B). Next 100 mL of DI water was poured in a 400-mL beaker (solution C) and its temperature was stabilized at 5, 25 or 55°C throughout the duration of the synthesis. Once the temperature of solution C reached its targeted value, solutions A and B were added simultaneously to it at a feeding rate of 0.16 mL min^{-1}. The solution was stirred at 800 rpm to prevent settling. After the consumption of the metal ion and carbonate solutions (~1 h), the solution was stirred for several hours to promote spherical particle formation and enlarge particle diameter. Later, precursor particles were sieved using filtering paper with 1.5-μm pore size, rinsed with 1 L of DI water and put into drying oven at 120°C overnight.

Material Characterization

Crystal structure analysis of metal carbonate precursors was performed using PANalytical Empyrean x-ray diffractometer (XRD) using CuKα radiation. The diffraction patterns were collected between 2θ = 15° and 75° at a scan rate of 2° min^{-1}. The morphological features of materials were observed with ZEISS Supra 55 model field-emission scanning electron microscope (FESEM) operated at 20 kV. Energy dispersive spectroscopy (EDS) was used for chemical analysis and elemental mapping using Quanta 200 FEG. For inductively coupled–plasma mass spectrometry (ICP-MS) measurements, the precursor materials were initially dissolved in a mixture of HNO_3 and HCl acids under heating and pressure. After full dissolution of solid materials, the analysis was carried out with a NEXION 2000 P (Perkin Elmer). Infrared spectroscopy (Jasco FT/IR-6700) was used to determine the space group of the $LiMn_{1.6}Ni_{0.4}O_4$ powder.

Electrode Preparation and Electrochemical Testing

After drying, $Mn_{0.8}Ni_{0.2}CO_3$ and $Mn_{4/6}Ni_{1/6}Co_{1/6}CO_3$ precursor materials were mixed with the required amount of Li_2CO_3 in a mortar and pestle for 10 min, and heated to 800°C in air for 15 h to obtain crystalline $Li_{1.2}Mn_{0.54}Ni_{0.13}Co_{0.13}O_2$ cathode material. The cathode electrode was prepared by first mixing 600 mg of active material, 75 mg of Timcal Super C45 conductive carbon, 75 mg of polyvinylidene fluoride and 5 g of N-methyl-2-pyrrolidone (NMP) in a beaker. After 1 h of stirring at 500 rpm, about 20 mg of the slurry was cast onto pre-cleaned 1 cm^2 aluminum foil. The NMP solvent was removed after keeping the Al foil at 120°C overnight. The active material loading was about 2 mg cm^{-2}. Type 2032 coin cells were made in an argon-filled glovebox with H_2O and O_2 levels under 1 ppm, using 1 M $LiPF_6$ in EC-DMC electrolyte and Whatman glass separator. Constant current charge–discharge tests were performed at C /3 between 3.0 V and 4.9 V versus Li metal for the $LiMn_{1.6}Ni_{0.4}O_4$ cathode, 2.5 V and 4.8 V for the $Li_{1.2}Mn_{0.54}Ni_{0.13}Co_{0.13}O_2$ cathode, and 2.9 V and 4.8 V for the hybrid electrode (50 wt% $LiMn_{1.6}Ni_{0.4}O_4$ + 50 wt% $Li_{1.2}Mn_{0.54}Ni_{0.13}Co_{0.13}O_2$).

Results and Discussion

Morphological Studies

Since temperature is expected to have a significant influence on the physical and chemical properties of the precursor material, the synthesis was performed at three different temperatures, namely 5°C, 25°C, and 55°C. The SEM images of $Mn_{0.8}Ni_{0.2}CO_3$ samples from different temperatures are displayed in Fig. 1a–c. The 5°C sample contains distinct and spherical particles having a diameter of 1–3 μm. Compared to this sample, raising the temperature to 25°C increases the particle diameter to the 2–4 μm range. Some small degree of aggregation can also be noticed. However, the further enlargement of the spheres was not observed when the synthesis temperature was raised to 55°C. We rather saw aggregates consisting of large numbers of spheres or peanut-like particles. These peanut-like features stem from incomplete solid-state fusion of two or more spheres. The increased level of aggregation is attributed to an increased coalescence rate at higher temperatures.[15,16]

Besides its effect on the morphological characteristics of the precursor material, EDS analysis revealed that temperature has a significant influence on the chemical composition of final material. The results showed that mole percentage of manganese in samples synthesized at 5, 25 and 55°C were in fact 84%, 83% and 80%, respectively (see supplementary FigureS1). The targeted value of Mn/Ni=4/1 (i.e. 80% Mn) was reached only at 55°C. The larger than expected Mn concentration was reported previously.[17]After the synthesis of all three batches, the yield was calculated to get higher with temperature. Specifically, it was about 65% at 5°C, 85% at 25°C and 95% at 55°C. Here, the yield is defined as the weight of product after drying to the weight from theoretical calculations. The poor yield is mostly due to material loss during sieving process. Therefore, we speculate that Ni-richer smaller particles were lost during sieving of 5 and 25°C samples. Since 55°C sample consists of large agglomerates, it suffered a much smaller loss. Another explanation regarding higher Mn concentration in final product might be provided based on solubility product constants (K_{sp}) of $MnCO_3$ and $NiCO_3$. The K_{sp} of the former is about 100–1000 times smaller than that of the latter (~10^{-11} for $MnCO_3$ and ~$10^{-9}$for $NiCO_3$).[18] This fact suggests that manganese carbonate is more preferentially precipitated, thereby explaining larger manganese concentration in the precursor material than the original feeding stock.

In order to ascertain whether Mn and Ni atoms were uniformly distributed within spherical particles, EDS elemental mapping was performed on the sample prepared at 5ºC. This sample was chosen due to the lack of aggregation, enabling the study of individual spheres. The mapping results of the Mn and Ni elements are presented in Fig. 2. It is clear that both elements have a homogeneous distribution across the particles.

The standard syntheses were performed by the simultaneous addition of separate 2 M metal sulfate and 2 M sodium

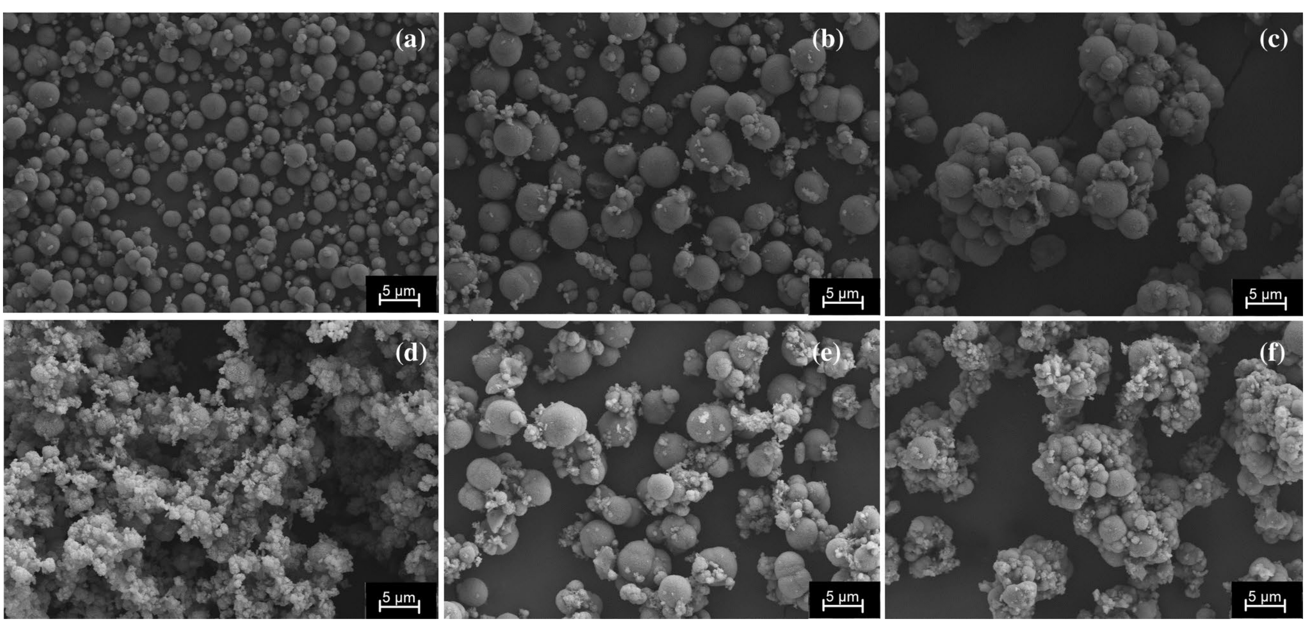

Fig. 1 SEM images of $Mn_{0.8}Ni_{0.2}CO_3$ powders synthesized at (a) 5°C, (b) 25°C, and (c) 55°C using a simultaneous addition route, (d) 25°C by pre-dissolved carbonate route, (e) 25°C with a final reagent concentration of 0.333 mol L^{-1} and (f) 0.667 mol L^{-1}.

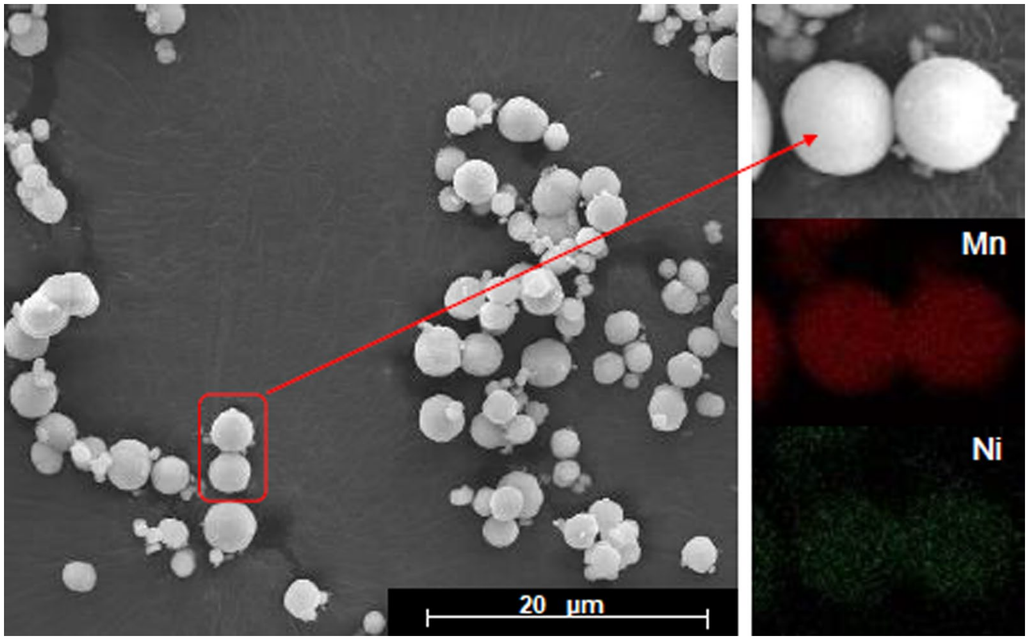

Fig. 2 EDS elemental mapping results of $Mn_{0.8}Ni_{0.2}CO_3$ prepared at 5°C.

carbonate solutions into 100 mL water. With each drop of ionic solutions, new nuclei form, collide with the previously formed larger ones and combine. This nucleation growth process ultimately yields the final spherical morphology. In order to alter the nucleation step, a different feeding mode was selected. In this new route (pre-dissolved carbonate), all the sodium carbonate solution was transferred into 100 mL water at once and then metal sulfate solution was added at a constant speed. The SEM image of the resulting material synthesized at 25°C is shown in Fig. 1d. The material is made of large number of sub-micron, rounded particles and there is no sign of discrete spherical particles but rather large aggregates. This is in strong contrast with the original route (simultaneous feeding), as shown in Fig. 1b. The smaller average particle size with the new route stems from its larger nuclei density. This argument is sound since there are much more available carbonate (CO_3^{-2}) ions at the beginning of the synthesis in the new route to react with the metal ions (Mn^{2+}, Ni^{2+}). And, as the feeding rate is constant, there will be a smaller quantity of reagent per nuclei to fuel their growth. This argument is consistent with earlier reports.[19,20]

Economically speaking, it is more desirable to synthesize as much material as possible in a single batch. With that goal, the impact of the overall reagent quantity per unit volume of batch was also studied. Here, the reagent quantity was defined as the ratio of the total mole of metal ions to the final volume of the batch. Besides the original 0.167 mol L^{-1}batch, two more with 0.333 mol L^{-1} and 0.667 mol L^{-1} values were also prepared. All three syntheses were carried out at 25°C and the combined total duration of the feeding and aging times was kept constant. The SEM photos of samples from 0.333 mol L^{-1} and 0.667 mol L^{-1} batches are provided in Fig. 1e and f, respectively. When the reagent quantity per volume is doubled from 0.167 mol L^{-1} to 0.333 mol L^{-1}, the most visible change is in the appearance of the aggregates. Also, the number of smaller spheres seems less due to their growth enabled by more reagent. With further doubling of the reagent quantity, no more discrete particles remain but instead large aggregates comprised of spheres with a wide size range emerge. The results indicate that the total material quantity per batch needs to be limited to avoid excessive aggregation of particles.

In order to electrochemically evaluate the spinel $LiMn_{1.6}Ni_{0.4}O_4$ and the layered–layered $Li_{1.2}Mn_{0.54}Ni_{0.13}Co_{0.13}O_2$ cathode materials, 55°C was selected as the synthesis temperature for the $Mn_{0.8}Ni_{0.2}CO_3$ and $Mn_{4/6}Ni_{1/6}Co_{1/6}CO_3$ precursors. This temperature was preferred to make sure that the Mn, Ni and Co ratios did not differ significantly from the intended values even though it came at the cost of having some aggregation. The elemental analysis of both precursor materials performed by ICP-MS revealed a final composition of $Mn_{0.79}Ni_{0.21}CO_3$ and $Mn_{0.653}Ni_{0.170}Co_{0.177}CO_3$ (see supplementary Figure S2), thereby proving that the final composition did not deviate much from the targeted numbers.

The morphological properties of the as-synthesized $LiMn_{1.6}Ni_{0.4}O_4$ and $Li1_{.2}Mn_{0.54}Ni_{0.13}Co_{0.13}O_2$ cathode materials were studied using SEM, and their images are presented in Fig. 3. Both samples maintained their spherical shape despite the high-temperature reaction with the lithium

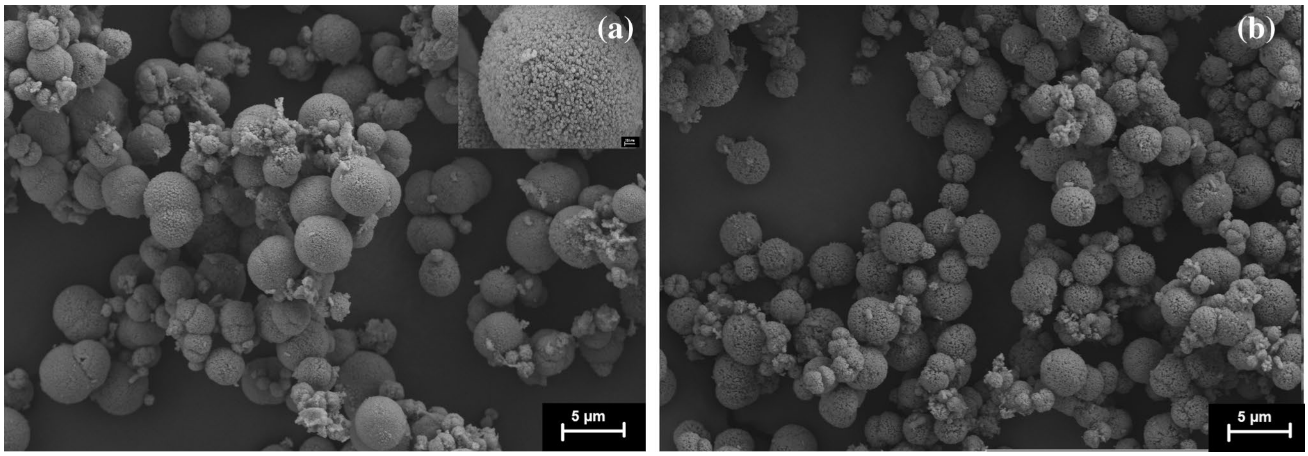

Fig. 3 SEM images of (a) $Li_{1.2}Mn_{0.54}Ni_{0.13}Co_{0.13}O_2$ (b) $LiMn_{1.6}Ni_{0.4}O_4$ powders.

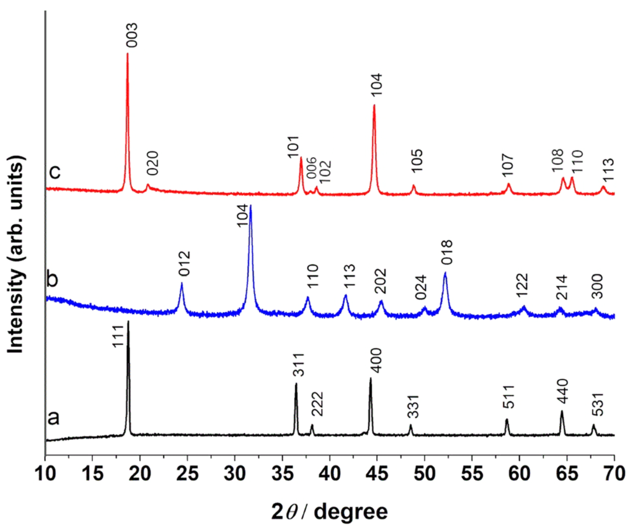

Fig. 4 XRD patterns of (a) $LiMn_{1.6}Ni_{0.4}O_4$, (b) $Mn_{4/6}Ni_{1/6}Co_{1/6}CO_3$ precursor material, and (c) $Li_{1.2}Mn_{0.54}Ni_{0.13}Co_{0.13}O_2$.

source. The spheres are about 3-4 μm in diameter and their surfaces are uniformly covered with 100-nm grains. The surfaces appear porous due to the removal of CO_2 from the carbonate precursor material during the high-temperature calcination step.

X-Ray Diffraction (XRD) Studies

The XRD pattern of the $LiMn_{1.6}Ni_{0.4}O_4$ cathode material is shown in Fig.4a. All the peaks match those of cubic spinel $LiMn_{1.5}Ni_{0.5}O_4$ (JCPDS: 80-2162).[21] The absence of any secondary peak suggests a single-phase nature of the cathode material. In the literature, the crystal lattice of this material is known to adopt two space groups, cation ordered $P4_332$ and cation disordered Fd3m.[22] It is also known that spinel belonging to Fd3m cycles better than $P4_332$.[22,23] In order to figure out the space group of our $LiMn_{1.6}Ni_{0.4}O_4$spinel material, its Fourier transform infrared spectroscopy (FTIR) data were collected and are shown in supplementary Figure S3. The spectrum is a good match with the Fd3m space group.

The XRD pattern of $Mn_{4/6}Ni_{1/6}Co_{1/6}CO_3$ precursor material is presented in Fig. 4b. All the peaks belong to the $MnCO_3$ phase with the R3c space group (JCPDS: 44-1472).[18,24] The absence of a secondary phase indicates that the Ni and Co atoms are completely dissolved in this phase and homogeneously distributed. The $Mn_{4/6}Ni_{1/6}Co_{1/6}CO_3$ precursor material was later throughly mixed with the required amount of Li_2CO_3 and heated to 800°C for 15 h in air. The XRD pattern of the final $Li_{1.2}Mn_{0.54}Ni_{0.13}Co_{0.13}O_2$ cathode material is given in Fig. 4c. Again, all the peaks belong to a single phase of α-$NaFeO_2$ structure with trigonal R-3m symmetry.[25] The weak (020) reflection near 21° is indicative of a monoclinic Li_2MnO_3 component with the C2/m space group.[26,27] The good splitting of the (006)/(102) and (108)/(110) reflexes as well as the large ratio of (003) and (104) peak intensities suggest good crystallinity for the $Li_{1.2}Mn_{0.54}Ni_{0.13}Co_{0.13}O_2$ cathode.

Electrochemical Tests

The voltage profiles of the $LiMn_{1.6}Ni_{0.4}O_4$, $Li_{1.2}Mn_{0.54}Ni_{0.13}Co_{0.13}O_2$ and hybrid cathodes in the first 3 cycles are displayed in Fig. 5. The $LiMn_{1.6}Ni_{0.4}O_4$ spinel cathode has a first-cycle discharge capacity of 132 mAh g^{-1} with a coulombic efficiency of 89% (Fig. 5a). Its charge and discharge profiles are split into two distinct regions; a sloping line between 4.1V and 4.3 V and a flat plateau around 4.7 V. The low voltage section is due to a Mn^{3+}/Mn^{4+} redox couple.[28,29] The discharge capacity from this region is about 24% of overall capacity. This number is higher than the theoretically expected value of 16% based on the charge balance

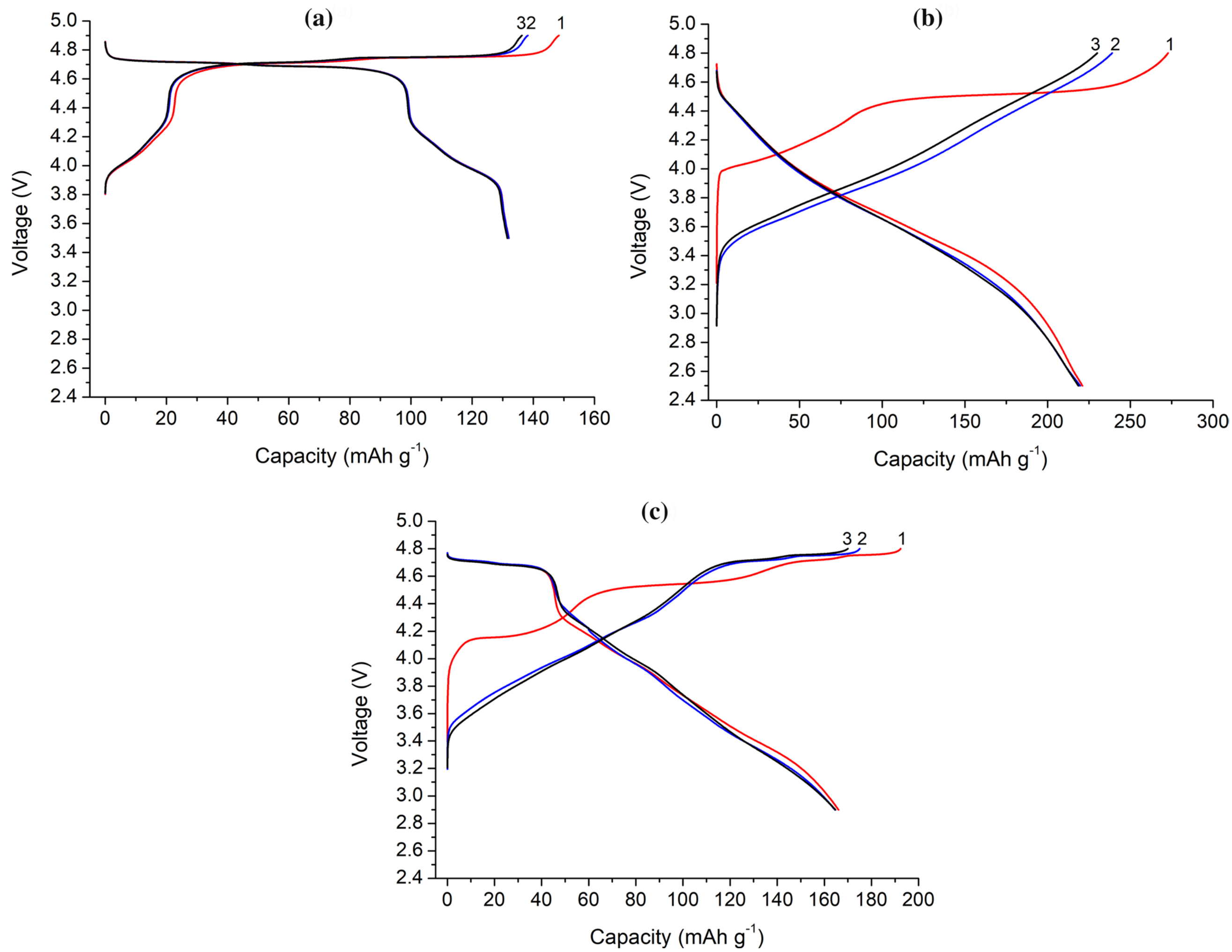

Fig. 5 Charge–discharge voltage profiles of 3 different cathodes in the first 3 cycles: (a) $LiMn_{1.6}Ni_{0.4}O_4$, (b) $Li_{1.2}Mn_{0.54}Ni_{0.13}Co_{0.13}O_2$, and (c) hybrid electrode (50:50 wt% of spinel and layered–layered cathodes).

of electrochemically active Mn^{3+} and Ni^{2+} ions in a spinel structure, i.e., $LiMn^{4+}_{1.42}Mn^{3+}_{0.16}Ni^{2+}_{0.42}O_4$ based on the ICP-MS result. The discrepancy is due to the reduction of some of the Mn^{4+} ions to the Mn^{3+} state resulting from oxygen loss during the high-temperature heat treatment.[30,31] A long plateau exists around 4.7 V attributed to Ni^{2+}/Ni^{+4} transitions. The splitting of this region is due to the separation of Ni^{2+}/Ni^{3+} and Ni^{3+}/Ni^{4+} redox pairs, consistent with earlier works.[28,32]

In the case of $Li_{1.2}Mn_{0.54}Ni_{0.13}Co_{0.13}O_2$, a sloping line between 4.0 and 4.5 V followed by a long flat plateau at 4.5 V is observed in the first-cycle charging step (Fig. 5b). The capacity from the sloping line is due to lithium extraction from the $LiNi_{1/3}Mn_{1/3}Co_{1/3}O_2$ component while the high voltage capacity is due to lithium removal from the Li_2MnO_3 component of the $Li_{1.2}Mn_{0.54}Ni_{0.13}Co_{0.13}O_2$ cathode. After this step, lithium insertion and removal take place along a sloping line consistent with the literature.[26,33,34] The first-cycle discharge capacity and coulombic efficiency of the $Li_{1.2}Mn_{0.54}Ni_{0.13}Co_{0.13}O_2$ cathode are 221 mAh g^{-1} and 81%, respectively.

The hybrid electrode consisting of equal weight percentages of both cathode materials reaches a maximum discharge capacity of 166 mAh g^{-1} with 86% first-cycle efficiency (Fig. 5c). The cut-off potential for discharging was limited to 2.9 V in order to prevent over-lithiation of $LiMn_{1.6}Ni_{0.4}O_4$ due to an intercalation reaction around 2.8 V.[35] Similarly, the charging cut-off potential was limited to 4.8 V in order to prevent excessive lithium removal from the layered–layered $Li_{1.2}Mn_{0.54}Ni_{0.13}Co_{0.13}O_2$ cathode, which is known to exacerbate capacity loss of layered material.[36] As a result of this, the discharge capacity of the hybrid electrode is 5-6% less than the arithmetic average of the mixture. Since spinel material operates in a high-to-medium voltage range and the layered–layered cathode operates in a medium-to-low voltage range, spinel particles will be lithiated first but only once the discharge is started. When the potential is low enough (i.e., below 4.5 V), lithiation of the layered–layered cathode particles will also start and both cathodes will carry the current load in parallel. At very low potentials (i.e., below 3.8 V), only $Li_{1.2}Mn_{0.54}Ni_{0.13}Co_{0.13}O_2$ contributes to the capacity. In summary, at very high and very low potentials, only one cathode material is active while a hybrid zone exists between 3.8V and 4.5 V where both cathodes operate in combination.

The variation of discharge capacities and average discharge voltages of all three cathodes are displayed in Fig. 6a, b for the first 100 cycles. The spinel cathode has an average discharge voltage of 4.525 V and maintains it without any degradation throughout the 100 cycles. The capacity loss at the end of this period is only 7.4%, thereby proving the excellent structural stability of this material. On the other hand, $Li_{1.2}Mn_{0.54}Ni_{0.13}Co_{0.13}O_2$ starts with a discharge potential of 3.623 V and gradually fades to 3.390 V after 100 cycles. Similarly, it undergoes a capacity loss of as much as 14.9%. Based on the average discharge potentials and specific discharge capacities at *C*/3, the specific energy density of the $LiMn_{1.6}Ni_{0.4}O_4$ cathode starts at 597 Wh kg^{-1} (4.525 V x 132 mAh g^{-1}) in the first cycle and ends with 553 Wh kg^{-1} at the end of the 100th cycle (92.6% retention). The same numbers correspond to 801 Wh kg^{-1} and 637 Wh kg^{-1} for $Li_{1.2}Mn_{0.54}Ni_{0.13}Co_{0.13}O_2$, respectively (79.5% retention). Finally, the hybrid cathode delivers an average discharge potential of 3.95 V and suffers a mere 60 mV loss, less than the arithmetic average of 115 mV. Also, the capacity loss is 9.4% which is closer to that of the spinel than the layered cathodes. In terms of energy density values, the hybrid electrode provides an energy density of 656 Wh kg^{-1} in the first cycle and finishes with 584 Wh kg^{-1} (89% retention). It is clear that a synergy is created when the two cathodes are coupled together and that the hybrid electrode over-performs relative to the arithmetic average of the individual cathodes. The underlying reason behind this over-performance of the hybrid electrode is as yet unknown to us, but it might be related to more conducive current distribution in the two-component system. This phenomenon deserves more scrutinized study both experimentally and theoretically.

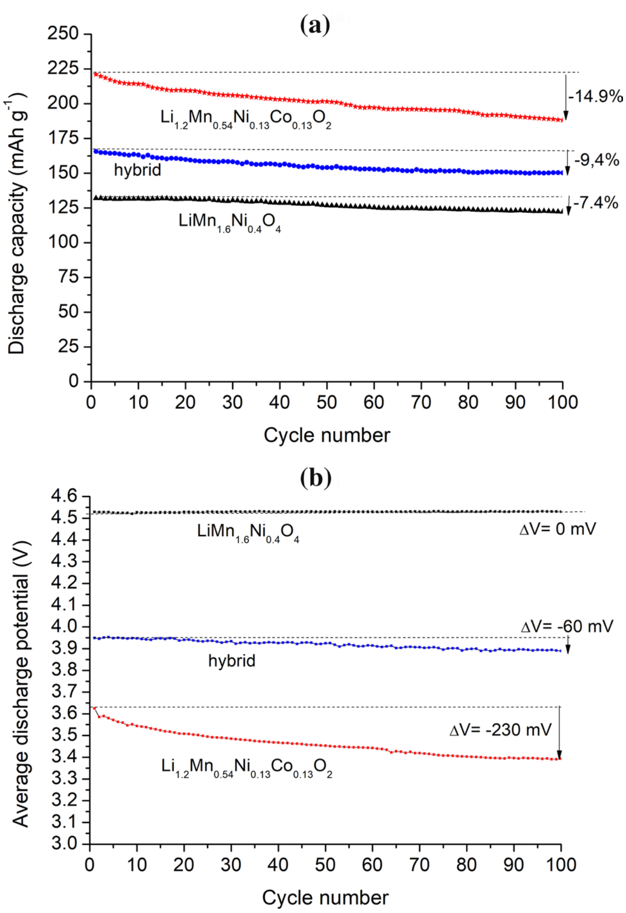

Fig. 6 (a) Variation of the discharge capacities of all three cathodes in the first 100 cycles. (b) Variation of average discharge potential of all three cathodes in the first 100 cycles.

Finally, all three electrodes were tested at 50 mA g^{-1}, 100 mA g^{-1}, 200 mA g^{-1}, and 400 mA g^{-1} current densities using sister cells to find out if this phenomenon will be extended to high-rate performances. The discharge voltage profiles of the three electrodes at different rates as well as their normalized capacities with respect to the capacity at 50 mA g^{-1} are presented in Fig. 7a–d. The spinel $LiMn_{1.6}Ni_{0.4}O_4$ cathode significantly out-performs the layered–layered $Li_{1.2}Mn_{0.54}Ni_{0.13}Co_{0.13}O_2$ at higher discharge rates thanks to the three-dimensionally open structure of the former to lithium intercalation. However, it is more interesting to see that the normalized capacities of the hybrid electrode again lie above those of the arithmetically expected values. It is also noticed that the difference gets smaller with increasing current density. The highlights of the battery test results of the three electrodes are summarized in Table I. The rate study further supports the above notion that a hybrid system might have a more beneficial current distribution within the electrode, thereby helping prolong its cyclability and improve its current-carrying capability.

Conclusions

Spherical, µm-sized $Li_{1.2}Mn_{0.54}Ni_{0.13}Co_{0.13}O_2$ and $LiMn_{1.6}Ni_{0.4}O_4$ cathode materials were synthesized using a coprecipitation method. The electrochemical tests showed that the spinel $LiMn_{1.6}Ni_{0.4}O_4$ cathode exhibits a stable, high-output voltage, and good capacity retention and rate performance. On the other hand, the layered–layered $Li_{1.2}Mn_{0.54}Ni_{0.13}Co_{0.13}O_2$ cathode offers a higher energy density but suffers from quick voltage fade and capacity loss. Given that these two cathodes have similar chemical

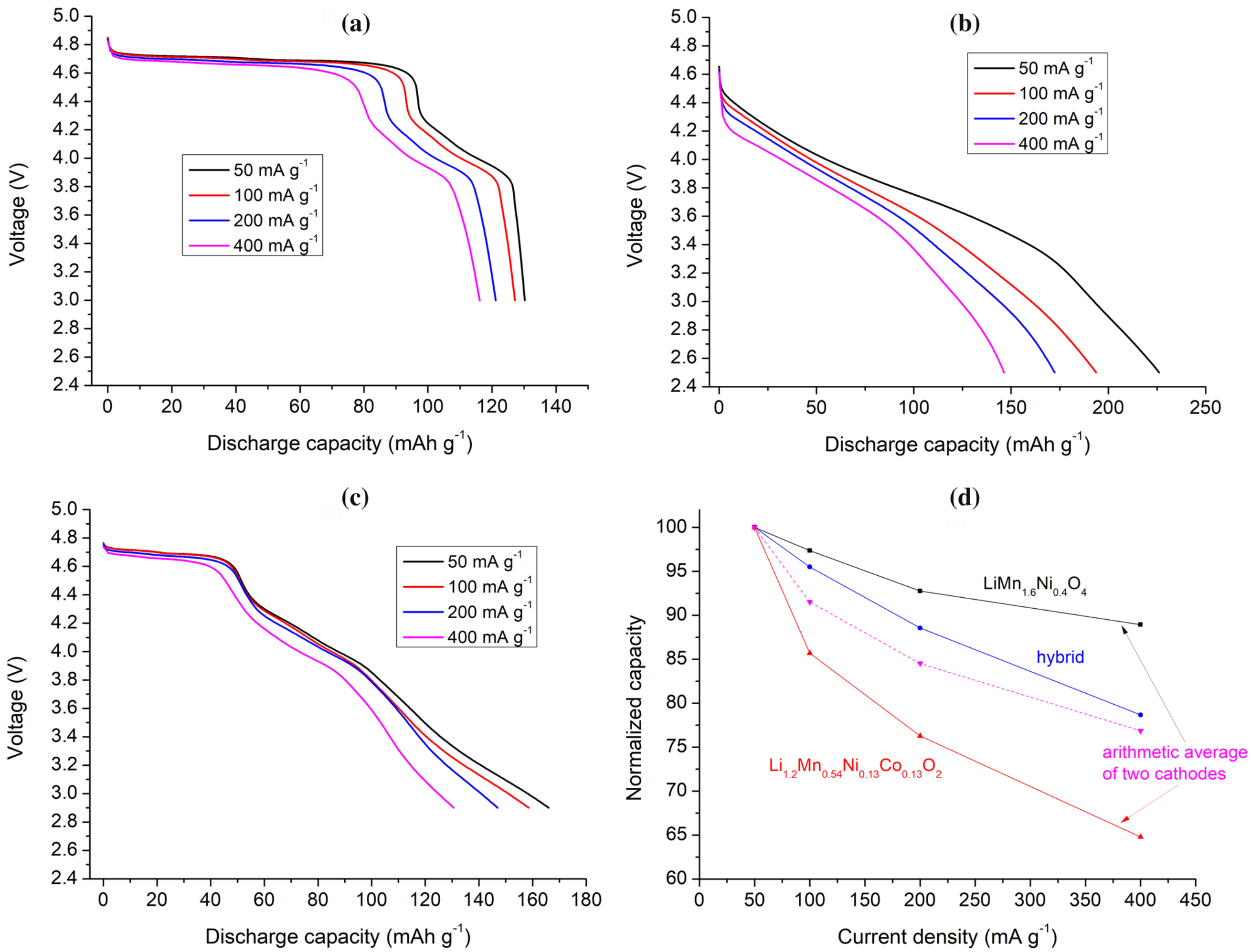

Fig. 7 Discharge voltage profiles at 50 mA g^{-1}, 100 mA g^{-1}, 200 mA g^{-1}, and 400 mA g^{-1} for (a) $LiMn_{1.6}Ni_{0.4}O_4$, (b) $Li_{1.2}Mn_{0.54}Ni_{0.13}Co_{0.13}O_2$, and (c) hybrid electrodes. (d) Normalized capacities of the three electrodes with respect to the capacity at 50 mA g^{-1}.

Table I Summary of battery test results for the three electrodes; the hybrid electrode performs better than the arithmetic average of the two cathodes in terms of voltage loss, capacity retention, and rate capability

	$LiMn_{1.6}Ni_{0.4}O_4$	$Li_{1.2}Mn_{0.54}Ni_{0.13}Co_{0.13}O_2$	Hybrid
1st-cycle discharge capacity	132 mAh g^{-1}	221 mAh g^{-1}	166 mAh g^{-1}
1st-cycle average discharge potential	4.525 V	3.623 V	3.95 V
1st-cycle coulombic efficiency	89%	81%	86%
Voltage loss after 100 cycles	0 mV	230 mV	60 mV
% capacity loss after 100 cycles	7.4%	14.9%	9.4%
(Capacity at 400 mA g^{-1}) / (Capacity at 50 mA g^{-1})	88.9%	64.8%	78.7%

fingerprints, their cost structure and synthesis route can be expected to be very similar. Also, they operate within the same voltage range. Therefore, a 50:50 wt% mixture was prepared with the hope of creating synergy between the two cathode materials. Indeed, the resulting hybrid electrode demonstrated a better cycle life, rate performance, and voltage loss than arithmetically expected. The average discharge voltage of 3.95 V and discharge capacity of 166 mAh g^{-1} of the hybrid electrode can be further improved by optimizing the individual cathode materials and electrode configuration.

Supplementary Information The online version contains supplementary material available at https://doi.org/10.1007/s11664-021-09357-x.

Acknowledgments This project received financial support from TUBITAK under the project number of 217M113 and from Mersin University under the project number of BAP-2020-1-TP2-4039. The authors would like to thank Ugur Caglayan from Cukurova University for ICP-MS and FTIR measurements.

Funding Tubitak, 217m113, Muharrem Kunduraci, Mersin Üniversitesi, Bap-2020-1-Tp2-4039, Rojbin Buluttekin.

Conflıct of ınterest The authors of this article declare that they have no conflict of interest.

References

1. K. Liu, B. Kong, W. Liu, Y. Sun, M.S. Song, J. Chen, Y. Liu, D. Lin, A. Pei, and Y. Cui, *Joule* 2, 1857 (2018).
2. W. Liu, J. Chen, Z. Chen, K. Liu, G. Zhou, Y. Sun, M.S. Song, Z. Bao, and Y. Cui, *Adv. Energy Mater.* 7, 1701076 (2017).
3. S.M. Xu, X. Liang, X.Y. Wu, S.L. Zhao, J. Chen, K.X. Wang, and J.S. Chen, *Nat. Commun.* 10, 5810 (2019).
4. H. Yin, K.S. Hui, X. Zhao, S. Mei, X. Lv, K.N. Hui, J. Chen, and A.C.S. Appl, *Energy Mater.* 3, 6897 (2020).
5. G. Zan, T. Wu, P. Hu, Y. Zhou, S. Zhao, S. Xu, J. Chen, Y. Cui, and Q. Wu, *Energy Storage Mater.* 28, 82 (2020).
6. N. Zhang, F. Huang, S. Zhao, X. Lv, Y. Zhou, S. Xiang, S. Xu, Y. Li, G. Chen, C. Tao, Y. Nie, J. Chen, and X. Fan, *Matters* 2, 1260 (2020).
7. R. Zhang, V. Raveendran, Y. He, A. Yau, A. Chang, C. Chi, S. Bong, F. Cheng, W. Ma, and J. Chen, *Energy Mater. Adv.* 2021, 1 (2021).
8. F. Wu, Z. Wang, Y. Su, Y. Guan, Y. Jin, N. Yan, J. Tian, L. Bao, and S. Chen, *J. Power Sour.* 267, 337 (2014).
9. M. Lengyel, G. Atlas, D. Elhassid, P.Y. Luo, X. Zhang, I. Belharouak, and R.L. Axelbaum, *J. Power Sour.* 262, 286 (2014).
10. Z. Wang, X. Cheng, W.J. Qiang, and B.X. Huang, *Cer. Int.* 45, 20016 (2019).
11. L. Yu, Y. Cao, H. Yang, and X. Ai, *J. Solid State Electrochem.* 10, 283 (2006).
12. N.V. Kosova, I.A. Bobrikov, O.A. Podgornova, A.M. Balagurov, and A.K. Gutakovskii, *J. Solid State Electrochem.* 20, 235 (2016).
13. J. Helbig, T. Beuse, V. Siozios, T. Placke, M. Winter, and R. Schmuch, *Electrochim. Acta* 366, 137413 (2020).
14. H. Zheng, Z. Hu, P. Liu, W. Xu, Q. Xie, W. He, Q. Luo, L. Wang, D. Gu, B. Qu, Z.Z. Zhu, and D.L. Peng, *Energy Storage Mater.* 25, 76 (2020).
15. M. Winkelmann, E.M. Grimm, T. Comunian, B. Freudig, Y. Zhou, W. Gerlinger, B. Sachweh, and H.P. Schuhmann, *Chem. Eng. Sci.* 92, 126 (2013).
16. K.E.J. Lehtinen, and M.R. Zachariah, *J. Aerosol Sci.* 33, 357 (2002).
17. Z. Zhu, D. Zhang, H. Yan, W. Li, and L. Qi, *J. Mater. Chem. A* 1, 5492 (2013).
18. Y. Xiang, Z. Yin, and X. Li, *Ionics* 20, 163 (2014).
19. H. Zhu, E.W. Stein, Z. Lu, Y.M. Lvov, and M.J. McShane, *Chem. Mater.* 17, 2323 (2005).
20. J.P. Robinson, and G.M. Koenig, *Powder Tech.* 284, 225 (2015).
21. C. Gao, H. Liu, S. Bi, S. Fan, X. Meng, Q. Li, and C. Luo, *J. Materiomics* 6, 712 (2020).
22. M. Kunduraci, and G.G. Amatucci, *J. Electrochem. Soc.* 153, A1345 (2006).
23. G. Liu, K.S. Park, J. Song, and J.B. Goodenough, *J. Power Sour.* 243, 260 (2013).
24. R. Xing, R. Li, Y. Xu, B. Li, J. Liu, S. Liu, D. Luo, and L. Mao, *Ceram. Int.* 43, 14426 (2017).
25. Y. Li, X. Li, Z. Wang, and H. Guo, *J. Energy Chem.* 27, 447 (2018).
26. C.S. Johnson, N. Li, C. Lefief, J.T. Vaughey, and M.M. Thackeray, *Chem. Mater.* 20, 6095 (2008).
27. Y. Zhang, W. Zhang, S. Shen, X. Yan, A. Wu, R. Wu, and J. Zhang, *Electrochim. Acta* 256, 316 (2017).
28. T.F. Yi, and Y.R. Zhu, *Electrochim. Acta* 53, 3120 (2008).
29. C. Arbizzani, F.D. Giorgio, L. Porcarelli, M. Mastragostino, V. Khomenko, V. Barsukov, D. Bresser, and S. Passerini, *J. Power Sources* 238, 17 (2013).
30. D. Liu, J.P. Hamel, J. Trottier, F. Barray, V. Gariepy, P. Hovington, A. Guerfi, A. Mauger, C.M. Julien, J.B. Goodenough, and K. Zaghib, *J. Power Sources* 217, 400 (2012).
31. D.S. Lu, J.L. Li, J. He, R.R. Zhao, and Y.P. Cai, *J. Phys. Chem. C* 123, 8522 (2019).
32. M. Kunduraci, and G.G. Amatucci, *J. Power Sources* 165, 359 (2007).
33. H. Liu, Q. Su, C. Yuan, T. Yuan, Y. Gu, and H. Cui, *J. Appl. Electrochem.* 47, 691 (2017).
34. M. Wang, Y. Chen, M. Luo, and L. Chen, *J. Appl. Electrochem.* 46, 907 (2016).
35. R. Grissa, H. Martinez, S. Cotte, J. Galipaud, B. Pecquenard, and F.L. Cras, *Appl. Surf. Sci.* 411, 449 (2017).
36. Z. Wu, C. Cao, X. Yan, X. Zang, Y. Zhao, X. Ma, R. Liu, L. Hu, Y. Jiang, and S. Sun, *Electrochim. Acta* 302, 153 (2019).